Geophysical Journal International

Geophys. J. Int. (2020) **220,** 1379–1393
Advance Access publication 2019 November 15
GJI Seismology

doi: 10.1093/gji/ggz514

A new crustal shear-velocity model in Southwest China from joint seismological inversion and its implications for regional crustal dynamics

Yan Yang,[1] Huajian Yao,[1,2] Hanxiao Wu,[1] Ping Zhang[1,*] and Maomao Wang[3]

[1] *Laboratory of Seismology and Physics of Earth's Interior, School of Earth and Space Sciences, University of Science and Technology of China, Hefei* 230026*, Anhui, China*
[2] *CAS Center for Excellence in Comparative Planetology, China. E-mail:* hjyao@ustc.edu.cn
[3] *College of Oceanography, Hohai University, Nanjing* 210098*, China*

Accepted 2019 November 15. Received 2019 July 29; in original form 2019 May 2

SUMMARY

Southwest (SW) China is located in a transition site from the active Tibetan Plateau to the stable Yangtze craton, which has complicated tectonic deformation and severe seismic hazards. We combine data from ambient noise, teleseismic body and surface waves, and petroleum wells and seismic-reflection profiles to better constrain the crustal shear velocity structure in SW China. We jointly invert the Rayleigh wave dispersion (5–40 s period), Rayleigh wave ZH ratio (20–60 s period), and *P*-wave receiver function for 114 permanent stations with a stepwise linearized joint inversion method. Compared to previous tomography results, we observe higher shear velocity in the sedimentary rocks within the Sichuan Basin, which is consistent with sonic logging measurements. Our model reveals widespread low-velocity zones in the mid-lower crust, and their boundaries correlate well with major fault systems. Between two main mid-crustal low-velocity channels, a prominent high-velocity region surrounded by earthquakes is observed in the inner zone of the Emeishan large igneous province (ELIP) and around the Anninghe-Zemuhe fault zone. These observations are comparable to regional tomography results using very dense arrays. Based on the results, we suggest that mid-lower crustal ductile flow and upper-crustal rigid fault movement play equally important roles in controlling the regional deformation styles and earthquake distribution in SW China. Our results also resolve thick crust–mantle transition zones beneath the eastern Tibetan Plateau and the inner zone of the ELIP due to 'top-down' and 'bottom-up' crust–mantle interactions, respectively. Our new model can serve as a reference crustal model for future high resolution model construction in SW China.

Key words: Joint inversion; Crustal imaging; Surface waves and free oscillations; Crustal structure; Large igneous provinces.

1 INTRODUCTION

Southwest (SW) China, which mainly consists of Sichuan and Yunnan Provinces, is located in a transition site from the southeastern margin of the Tibetan Plateau in the west to the Yangtze Craton in the east (Fig. 1). Three major fault systems are present in this region: the left-lateral Xianshuihe-Xiaojiang fault, the right-lateral Red River fault and a complex of left-lateral and normal faults in the Dali fault system (Wang 1998; Wang & Burchfiel 2000). These major fault systems and the Longmenshan fault accommodate most of the large earthquakes in the region and separate the area into different tectonic units (Fig. 1b). The main tectonic units in this region are the lens-shaped Chuandian block, which is bounded by the three fault systems; the Songpan-Ganzi fold belt (SGFB) in the north; the Yangtze craton (YC) in the east; the Qiangtang block (QB) and the Lhasa block (LB) in the west and the Shan Thai block (STB) in the south (Fig. 1b).

Seismologically, SW China is located in the southern-central portion of the China north–south Seismic Zone, a severe earthquake hazard zone (Zhang *et al.* 2003). More than one-third of documented historical large earthquakes ($M_w > 7$) in China occurred in this region (Zhang 2013, Fig. 1b). The devastating M_w 7.9 Wenchuan earthquake in 2008 further demonstrates this strong seismic activity. Tectonically, this region marks the boundary between the highly

---

[*] Now at Research School of Earth Sciences, Australian National University, ACT, Australia.

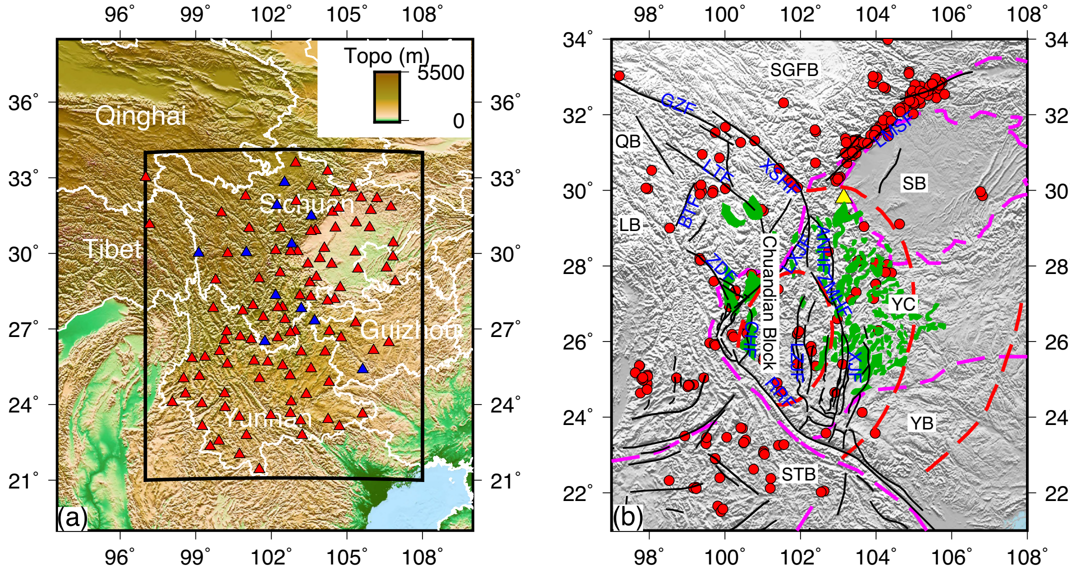

Figure 1. (a) Topography map of SW China and adjacent areas. The white lines show provincial boundaries in China; the triangles show 114 permanent stations used in joint inversion, where red indicates the use of direct ZH ratio measurements while blue indicates the use of ZH ratio interpolated with other stations; The black box outlines the study region as shown in (b). (b) Tectonic elements and fault systems in the study region. The dashed magenta lines show tectonic boundaries. The solid black lines show major faults. The red filled circles show epicentres of earthquakes ($M_\mathrm{w} > = 5.0$) between 1980 and 2016. The yellow triangle denotes the location of the Emei Mountain. The green shaded area shows the distribution of basalts and the red dashed lines outline the boundary between the inner, intermediate, and outer zones of ELIP (Xu *et al.* 2004). SGFB, Songpan-Ganzi fold belt; QB, Qiangtang block; LB, Lhasa block; SB, Sichuan basin; YC, Yangtze craton; YB, Youjiang block; STB, Shan Thai block; GZF, Ganzi fault; LTF, Litang fault; BTF, Batang fault; LMSF, Longmenshan fault; XSHF, Xianshuihe fault; ZDF, Zhongdian fault; ANHF, Anninghe fault; CHF, Chenghai fault; LZJF, Lüzhijiang fault; ZMHF, Zemuhe fault; LXJF, Lijiang-Xiaojinhe fault; XJF, Xiaojiang fault; RRF, Red River fault.

deforming Tibetan Plateau and the stable Yangtze craton. The Tibetan Plateau is the product of the collision between the Indian and Eurasian plates during the Cenozoic, with intense surface uplift and crustal shortening and thickening (Molnar & Tapponnier 1975; Yin & Harrison 2000). Two popular and competing models have been proposed to explain the tectonic evolution and crustal deformation of the plateau: the lateral extrusion of rigid blocks along large strike-slip faults (Tapponnier *et al*. 1982, 2001) and crustal channel flow in the weak zones of mid-lower crust (Royden 1997; Clark & Royden 2000; Royden *et al.* 2008). GPS measurements indicate clockwise surface material transport from southern or central Tibet to SW China (Zhang *et al.* 2004). However, the transport of deep crustal and mantle material remains elusive. Therefore, a detailed investigation on the crustal structure in SW China may play a key role in assessing seismic hazards and discriminating between these competing models.

Previous geophysical works applied various tools to investigate the crustal structure beneath SW China. Widespread low velocity zones (LVZ) in the middle to lower crust have been confirmed by *P*- and *S*-wave traveltime tomography (Huang *et al.* 2002, 2015; Wang *et al.* 2003), ambient noise tomography (Yao *et al*. 2006, 2008; Li *et al.* 2009; Huang *et al.* 2010; Yang *et al.* 2012), receiver function imaging (Zhang *et al.* 2010; Wang *et al.* 2017; Hu *et al.* 2018) and deep seismic soundings (Wang *et al.* 2007; Zhang & Wang 2009; Zhang *et al.* 2011). High electrical conductivity (Bai *et al.* 2010; Rippe & Unsworth 2010), high surface heat flow (Hu *et al.* 2000; Jiang *et al.* 2019), high attenuation (Bao *et al.* 2011; Zhao *et al.* 2013) also support the existence of mechanically weak zones. These findings favour the existence of regional crustal channel flow to some degree. However, the uneven distribution of these weak crustal zones, some of which are bounded by major fault zones, also reveals the significant effect of the large fault zones (Yao *et al*. 2008, 2010; Liu *et al.* 2014; Qiao *et al.* 2018). The validity of unhindered lower-crustal flow in SE Tibet as proposed in earlier models (Royden 1997; Shen *et al.* 2001; Cook & Royden 2008) is also questioned by local studies on the Emeishan large igneous province (ELIP). The ELIP, which is bounded by the Longmenshan fault to the northwest and the Red River fault to the southwest (Fig. 1b), is generally believed to be associated with an ancient mantle plume (Xu & Chung 2001; Ali *et al.* 2010). Multidisciplinary studies have revealed high shear velocity (V_S), high compressional velocity (V_P), high V_P/V_S ratios, high density, high strength and low heat flow in the crust of the inner zone of the ELIP (He *et al.* 2003; Deng *et al.* 2014, 2016; Chen *et al.* 2015; Xu *et al.* 2015), in sharp contrast to the weak zones in the mid-lower crust in the Tibetan Plateau. Therefore, some recent studies suggested that the strong crust of the inner zone of the ELIP probably bifurcates the transport of weak crustal material into two major channels around the ELIP (Qiao *et al.* 2018).

A number of 3-D shear velocity models in SW China have been proposed with different data sets, for example body waves (Huang *et al.* 2015; Xin *et al.* 2019), surface waves (Yao *et al.* 2010; Shen *et al.* 2016; Qiao *et al.* 2018) and the joint inversion of surface wave dispersion and receiver function (RF, Liu *et al.* 2014; Bao *et al.* 2015). These models are similar to some degree but differ in many details, probably due to the non-uniqueness in inversion or differences in data sensitivities. In this study, we aim to provide a model that can fit more data sets with consistent and complementary sensitivities to the crust. Surface wave dispersion can constrain the smooth variation of absolute shear velocity structures, whereas RFs are sensitive to discontinuities in the crust and upper mantle. Thus, the joint inversion of surface wave dispersion and RFs has long been considered an effective method of mapping V_S structures (e.g. Julia *et al.* 2000; Shen *et al.* 2013). The Rayleigh-wave ZH ratio (the amplitude ratio between the vertical and horizontal components of fundamental-mode Rayleigh waves) provides localized structural constraints beneath a station, similar to RF (Chong *et al.* 2016). The ZH ratio is very sensitive to shallow crustal structures, of which the depth extent of sensitivity kernels is approximately half that of Rayleigh-wave dispersion at the same period (Tanimoto & Rivera 2008; Yano *et al.* 2009). Therefore, the ZH ratio can provide complementary information for crustal structure inversion. Additionally, errors in the shallow crust may leak into the mid-lower-crustal velocity structure in the inversion. Thus, a fine and reliable basin velocity model can offer better initial information for the inversion.

In this paper, we first measure Rayleigh wave dispersion data (period band of 5–40 s) from ambient noise analysis, Rayleigh wave ZH ratio measurements (period band of 20–60 s) from teleseismic surface waves, and teleseismic *P*-wave RFs by using waveform data that predominantly originated from the permanent stations in SW China. We also combine a smooth shear velocity model from surface wave tomography (Shen *et al.* 2016) and a recent Sichuan Basin velocity model that was mainly derived from industrial oil wells (Wang *et al.* 2016) as an initial model to improve the final inversion results. Then, we adopt a stepwise linearized inversion algorithm (Zhang & Yao 2017) to jointly invert three data sets for the 1-D shear wave velocity model at each station, which is finally combined into a new 3-D shear-velocity model in SW China. Finally, we discuss the tectonic implications of our new model.

2 DATA PROCESSING

We used the ambient noise, teleseismic body and surface wave data recorded by the permanent broadband stations from the China National Seismic Network (Zheng *et al.* 2010) in our study region (97°E–108°E, 21°N–34°N). Because our available data were requested in different time, the stations with any individual type of data do not completely overlap. Therefore, in this paper we only presented inversion results of a total of 114 permanent stations (Fig. 1a), although the number of the stations that we used to process any individual type of data is larger than 114. These 114 stations have both RF and ZH ratio measurements, and the phase velocity maps can be interpolated onto the location of these stations. The details of the data processing are described in this section.

2.1 Rayleigh wave dispersion

We processed vertical-component continuous seismic waveforms that were recorded from September 2008 to December 2009 by 124 permanent broad-band stations. The waveforms were cut into 1-d-long time-series and downsampled to 5 Hz. We followed the ambient noise data-processing procedure in Zhang *et al.* (2018) to compute the interstation noise cross-correlation functions (NCFs): removal of the instrument response, means and trends; spectral whitening for each 2-hr-long waveform segment; connection of the 2-hr-long processed waveforms to get a 1-d-long time-series; multiple period-band running-absolute-mean normalization for each daily waveform; the combination of multiple-band normalized waveforms into broad-band waveforms (period band of 5–40 s); and cross-correlation. The NCFs were linearly stacked from daily NCFs for each station pair. The empirical Green's function (EGF) can be then extracted from NCFs (Snieder 2004; Yao *et al.* 2006). Following previous studies (Yao *et al*. 2006, 2011), we extracted the interstation phase velocity dispersion curves from the EGFs under the far-field assumption of the surface wave Green's function. The selection of acceptable measurements was based on two criteria: (1) the distance between the pair of stations should be larger than twice the wavelength; (2) the signal-to-noise ratio (SNR) of the EGF should be larger than five. We also adopted the cluster analysis of dispersion curves from similar paths to eliminate outliers (Zhang *et al.* 2018).

To improve the ray path coverage in the northwestern and southeastern portions of the study region, we augmented the interstation phase velocity dispersion curves of 35 temporary stations in SE Tibet that were deployed by MIT and Lehigh University in 2003–2004 (Yao *et al.* 2010), 16 temporary stations in northern Vietnam that were deployed by the Institute of Earth Sciences of Academia Sinica in Taiwan in 2008 (Nguyen *et al.* 2013) and 49 stations in Yunnan (Qiao *et al.* 2018; Figs 2a and 3a). Finally, we collected nearly 7000 Rayleigh-wave phase velocity dispersion curves in the period band of 5–40 s (Fig. 2).

With the extracted Rayleigh wave dispersion curves, we constructed 2-D phase velocity maps at different periods with 0.25° × 0.25° grid points based on continuous regularization (Tarantola & Valette 1982; Liu & Yao 2017). We performed a checkerboard test to determine the lateral resolution for each period. Anomalies of 5 per cent amplitude and 1° × 1° size could be resolved at 10 s (Fig. 3b). Based on these checkerboard tests, we chose the correlation length for each period, which determines the smoothness of the phase velocity maps (Fig. 2b). Next, we constructed phase velocity maps from 5 to 40 s with an interval of 1 s. We defined the data variance of the phase velocity from the *a posteriori* covariance matrix obtained in the tomography (Tarantola & Valette 1982). The data variance with the value less than 1 per cent of the phase velocity was set as 1 per cent of the phase velocity. The isotropic phase velocity map at 10 s is shown in Fig. 3(c). Two prominent anomalies are the low-velocity anomaly in the northwestern Sichuan Basin and the high-velocity anomaly in the inner zone of the ELIP.

2.2 Rayleigh wave ZH ratio

We used 512 earthquakes with magnitudes of $M_w \geq 5.5$ in 2014 and 2015 recorded at 118 permanent stations in our study region. For each earthquake, we applied the automated frequency-time analysis (FTAN) method (Bensen *et al.* 2007) to measure the Rayleigh wave amplitudes of both the vertical and radial components for all stations. The ZH ratio measurements were determined at periods between 20 and 100 s. The Rayleigh wave dispersion that we used in this study was limited to the period range of 5–40 s, so we only used the ZH ratio measurements in the 20–60-s period to jointly constrain the crustal and uppermost-mantle structures.

Following Lin *et al.* (2012) and Yuan *et al.* (2016), we imposed several selection criteria in data processing to avoid potential bias and improve the reliability of the measurements. The criteria include the following: (1) measurements with SNRs smaller than 15 on any component were removed; (2) ZH ratio measurements smaller than 0.6 or larger than 1.8 were removed; (3) measurements with $|\tau_Z - \tau_R - T/4| > 10$ were removed, where τ_R and τ_Z are the traveltimes that were measured on the radial and vertical components and T is the period; (4) for each period, the corresponding mean value and the standard deviation of the mean value were calculated if the number of earthquakes that were recorded at this period was more than 30 and (5) for each period, all ZH ratio measurements outside the 2σ range were removed. Then, the mean and standard deviation for the retained data were calculated again.

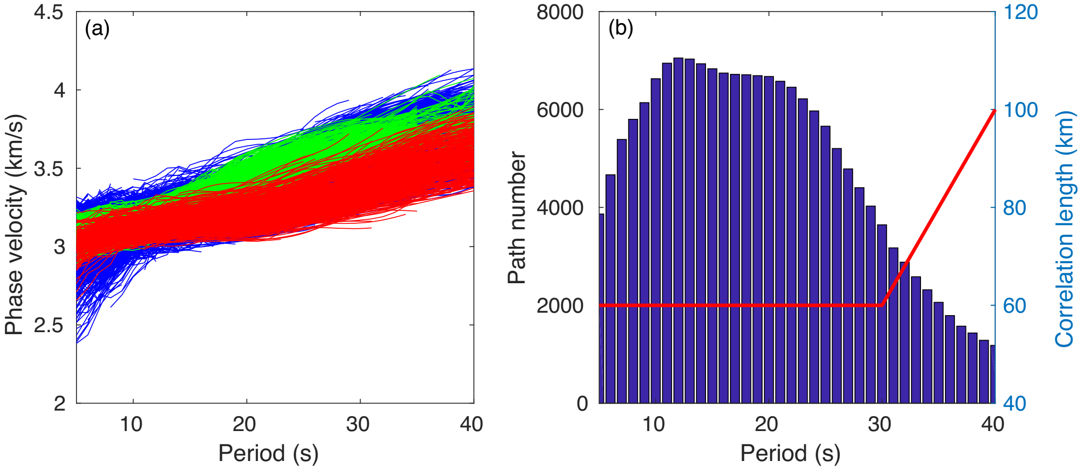

Figure 2. (a) Rayleigh wave phase velocity dispersion curves from different data sets. The blue lines represent data from permanent stations from the China National Seismic Network. The green lines represent data from the temporary stations in northern Vietnam and Yunnan. The red lines represent data from MIT and Lehigh University stations. (b) Number of paths (blue bars) and correlation length of each period (red line) in 2-D phase velocity map construction.

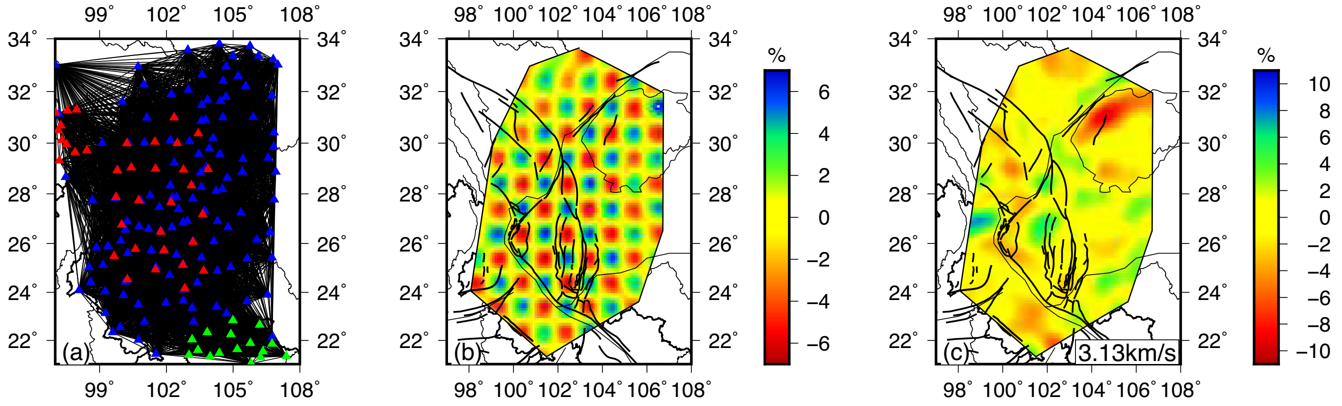

Figure 3. (a) Path coverage at 10 s. The blue triangles show the 124 permanent stations that were used for ambient noise cross-correlation. The red and green triangles denote the temporary stations that were deployed by MIT and Lehigh University and the temporary stations in northern Vietnam, respectively. (b) Recovered isotropic phase velocity map at 10 s with the input 1° × 1° checkerboard anomalies. (c) Phase velocity variation (in per cent) with respect to the mean velocity at 10 s. The number on the right bottom means the average phase velocity.

If the ZH measurements at each period nearly satisfied the Gaussian distribution, the obtained results were considered reliable. We used the mean value as the ZH ratio value at this period and the standard deviation of the mean value as the data variance. The data variance with the value less than 2 per cent of the ZH ratio value was set as 2 per cent of the ZH ratio value. Fig. 4 shows an example of the ZH ratio measurements at a 25-s period for the station YUJ. ZH ratios that are measured from either earthquake surface waves or ambient noise usually have substantial variability. Any uncertainty is suggested to be caused by effects from small-scale heterogeneity (Ferreira & Woodhouse 2007). Some researchers believe that this type of variability is stable and can be solved statistically (Tanimoto & Rivera 2008).

Compared to the Rayleigh wave phase velocity, whose peak sensitivity to V_S is at a depth of approximately a third of its wavelength (Lin *et al.* 2012), the sensitivity kernel of the ZH ratio to V_S peaks in the upper few kilometres even for long periods (Fig. 5). The interpolated 2-D ZH ratio maps at periods of 25 and 40 s and their uncertainties are plotted in Fig. 6. For both periods, the prominent feature is the low ZH ratios in the Sichuan Basin, which could be attributed to the horizontal amplification of surface waves in sediments.

2.3 RF data

We selected 668 teleseismic events in 2015 and 2016 with magnitudes of $M_w \geq 5.5$ and epicentral distances within 30°–90°, which were recorded at 140 permanent stations in our study region, to calculate the *P* wave RFs (e.g. Fig. 7). The backazimuths of these events predominantly ranged from 30° to 150° (Fig. 7a). The raw data were cut in a time window of [–30 s, 120 s] relative to the direct *P*-wave arrival time that was calculated with the IASP91 model (Kennett & Engdahl 1991), resampled to 10 Hz and bandpass filtered in a frequency band of [0.1, 1] Hz. Waveforms with unrecognized *P* phases or low SNRs were discarded. Then, we used the time-domain iterative deconvolution method (Ammon 1991) to calculate RFs, with a Gaussian width of 2.5. Following Shen *et al.* (2013), we removed RFs whose variance reduction in the iterative deconvolution was less than 80 per cent. RFs with negative amplitude at zero time and abnormally large energy were also removed. We further visually inspected the RF waveforms of all stations by the Funclab package (Eagar & Fouch 2012). Finally, about 150 traces for each station were kept for further analysis. To remove any effects from different ray parameters, we performed moveout

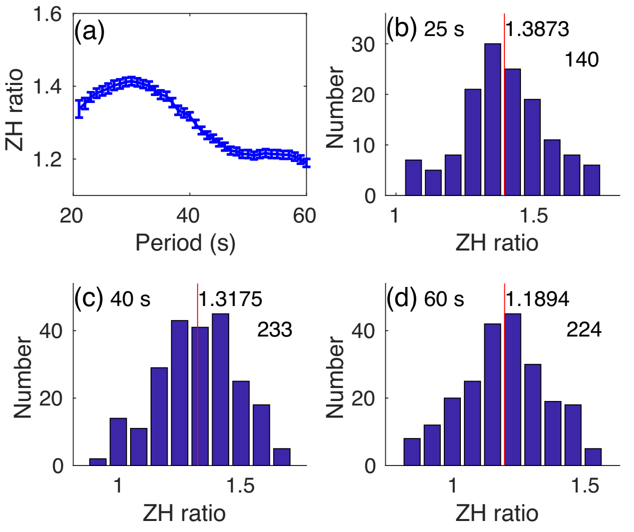

Figure 4. Example of ZH ratio measurements at station YUJ. (a) ZH ratio at periods of 20–60 s with the associated uncertainties plotted in error bars. (b–d) Distribution of ZH ratio measurements from different events at 20, 40 and 60 s. The red lines denote the mean of all measurements, with the mean value labeled on the top and the total number of events marked on the right.

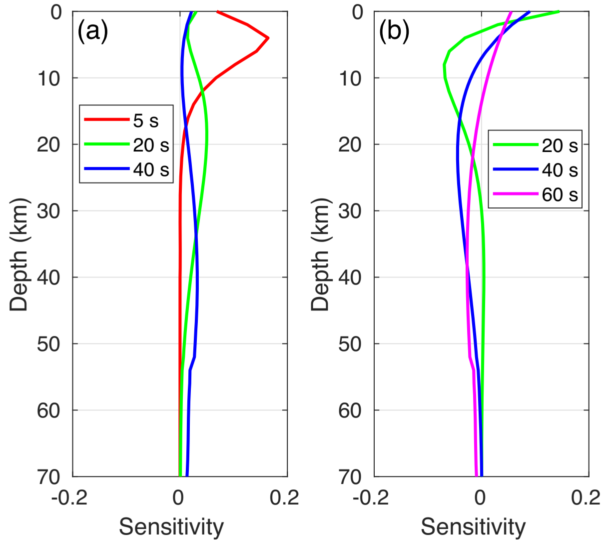

Figure 5. Depth sensitivity to V_S of the (a) Rayleigh wave phase velocity (5, 20, 40 s) and (b) ZH ratio (20, 40, 60 s). These sensitivities were computed based on the resulting model at station LTA in Fig. 7.

correction to an epicentral distance of 60° and a source depth of 0 km (ray parameter of 6.8 s deg^{-1}) according to the Preliminary Reference Earth Model (PREM, Dziewonski & Anderson 1981). We only kept 10 s after *P* onset for RF waveforms for the joint inversion with surface wave dispersion data (5–40 s) to recover the crustal and uppermost-mantle structures.

Three examples of RFs (Fig. 7) at different locations display distinct variations in *Pms* phase arrival time. The RF waveforms also have backazimuth dependence, which may be related to crustal anisotropy or a dipping interface. Therefore, we adopted harmonic decomposition to estimate the backazimuth dependence of the RFs (Shen *et al.* 2013; Liu *et al.* 2015). The RFs from all the backazimuths can be termed as a sum of cos($k\phi$) and sin($k\phi$), in which k denotes the harmonic order and ϕ denotes the backazimuth. The coefficients of the $k = 0, 1, 2$ terms $A(t)$, $B(t)$, $C(t)$, $D(t)$, $E(t)$ can be computed in a linear system:

$$\begin{bmatrix} R_1(t) \\ R_2(t) \\ \ldots \\ R_n(t) \end{bmatrix} = \begin{bmatrix} 1 & \cos(\phi_1) & \sin(\phi_1) & \cos(2\phi_1) & \sin(2\phi_1) \\ 1 & \cos(\phi_2) & \sin(\phi_2) & \cos(2\phi_2) & \sin(2\phi_2) \\ \ldots & \ldots & \ldots & \ldots & \ldots \\ 1 & \cos(\phi_n) & \sin(\phi_n) & \cos(2\phi_n) & \sin(2\phi_n) \end{bmatrix} \times \begin{bmatrix} A(t) \\ B(t) \\ C(t) \\ D(t) \\ E(t) \end{bmatrix}, \tag{1}$$

where n is the number of events, $R_i(t)$ are radial RFs with backazimuth ϕ_i at each time step t. $A(t)$, $B(t)$, $C(t)$, $D(t)$, $E(t)$ are the coefficients of the terms. The estimated RF with backazimuth of ϕ at time t can be computed as:

$$H_i(\phi, t) = A(t) + B(t)\cos(\phi) + C(t)\sin(\phi) + D(t)\cos(2\phi) + E(t)\sin(2\phi), \tag{2}$$

Usually the azimuthally independent term $A(t)$ represents the isotropic structure. In our study region, the azimuth distribution of events is uneven (Fig. 7). When the backazimuthal coverage of the RFs is sparse, the estimation of $A(t)$ cannot provide a good estimate of isotropic structure (Kang *et al.* 2016). Following Kang *et al.* (2016), we averaged $H_i(\phi, t)$ between 30° and 150° azimuth range instead of directly using $A(t)$ to provide a more repeatable and reliable representation of the local isotropic structure. Following Shen *et al.* (2013), we defined the data variance of RF using the RMS difference over azimuth between the observed receiver function $R_i(t)$ and the harmonic function $H_i(t)$.

2.4 Initial model in the Sichuan Basin

We incorporated the top 10 km of a new, high-resolution *P*-wave velocity model for the 20 stations in the Sichuan Basin (Wang *et al.* 2016) into the crustal and upper-mantle velocity model (Shen *et al.* 2016). The basin model was obtained from direct measurements from 36 sonic logs and seismic-reflection profiles (Wang *et al.* 2016). Rayleigh wave dispersion, the ZH ratio, and RFs are more sensitive to V_S than V_P, so we converted their V_P model into a V_S model using the V_S–V_P relationship from Wang *et al.* (2016). The V_S–V_P relationship was derived using the vertical seismic profiles data containing *P* and *S* wave measurements based on an empirical V_S–V_P relationship (Brocher 2005):

$$V_{S\_Brocher} = 0.0064V_P^4 - 0.1238V_P^3 + 0.7949V_P^2 - 1.2344V_P + 0.7858, \tag{3}$$

$$V_S = 0.8706V_{S\_Brocher} + 0.14785, \tag{4}$$

where V_P represents the *P*-wave measurements, $V_{S\_Brocher}$ represents the *S*-wave velocity that was computed with Brocher's empirical relationship, and V_S represents the predicted *S*-wave velocity we used in our initial model. The density in our model was also converted from V_P by using empirical relationships from Brocher (2005).

In Fig. 8, we compare the V_S at 1-km depth in the Sichuan Basin based on sonic logging measurements (Wang *et al.* 2016) with that from surface wave tomography (Shen *et al.* 2016). The V_S from the latter study in Fig. 8(c) is apparently lower than that from the former study in Fig. 8(a). We also plot the 1-D V_S model above

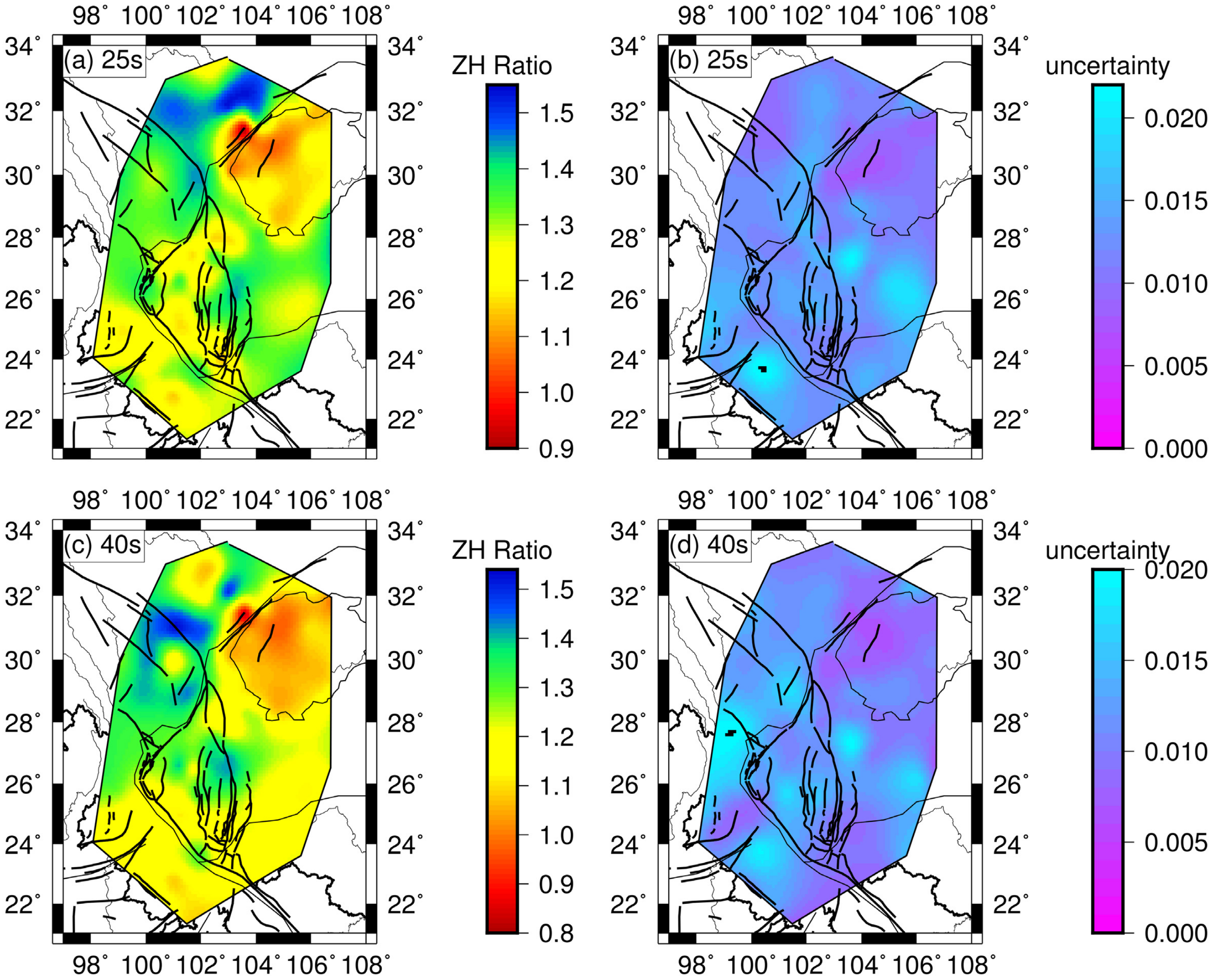

Figure 6. Example maps of the Rayleigh wave ZH ratio at (a) 25 s and (c) 40 s. The associated uncertainties are also presented in (b) and (d).

10-km depth and their data fitness to the RF and ZH ratio in both studies (Fig. 9). The predicted data with the model from Wang *et al.* (2016) fit the observations better than the model from surface wave tomography (Shen *et al.* 2016).

3 INVERSION METHOD

Following (Zhang & Yao 2017),we adopted a stepwise joint-inversion algorithm with Rayleigh wave dispersion, ZH ratios and RF data for a 1-D crustal and uppermost-mantle V_S structure for each station. The forward problem can be written as:

$$\boldsymbol{d} = \boldsymbol{G}(\boldsymbol{m}), \tag{5}$$

where $\boldsymbol{d}$ is the data vector of the three data types; $\boldsymbol{G}$ is the forward operator; $\boldsymbol{m}$ is the model vector consisting of layered V_S parameters beneath each station location. The inverse problem is to minimize the misfit function:

$$\phi(\boldsymbol{m}) = ||\boldsymbol{G}(\boldsymbol{m}) - \boldsymbol{d}||_2^2 + \eta^2||\boldsymbol{L}\Delta\boldsymbol{m}||_2^2, \tag{6}$$

where η is a smoothing parameter for the regularization; $\boldsymbol{L}$ is the model regularization matrix, which is chosen as the first-order Tikhonov regularization matrix in this study (Aster *et al.* 2013); $\Delta\boldsymbol{m}$ is the V_S model update (Zhang & Yao 2017). As shown in Zhang & Yao (2017), a linearized iterative damped least-squares algorithm was used to minimize the misfit function $\phi(\boldsymbol{m})$ through the weighted forward equation:

$$\begin{bmatrix} \theta\boldsymbol{G}_{Disp} \\ \varphi\boldsymbol{G}_{ZH} \\ \lambda\boldsymbol{G}_{RF} \\ \eta\boldsymbol{L} \end{bmatrix} \Delta\boldsymbol{m} = \begin{bmatrix} \theta\boldsymbol{r}_{Disp} \\ \varphi\boldsymbol{r}_{ZH} \\ \lambda\boldsymbol{r}_{RF} \\ 0 \end{bmatrix}, \tag{7}$$

where the weighting coefficients are given by

$$\theta^2 = \frac{p}{N_{Disp}\sigma_{Disp}^2}, \quad \varphi^2 = \frac{q}{N_{ZH}\sigma_{ZH}^2}, \quad \lambda^2 = \frac{r}{N_{RF}\sigma_{RF}^2}, \tag{8}$$

The subscripts $Disp$, ZH, RF represent the dispersion, ZH ratio and RF data, respectively; $\boldsymbol{r}$ represents the residual data vectors; θ, φ and λ are weighting coefficients; N represents data points; σ^2 represents data variance. p, q and r ($p+q+r = 1$) are the relative weights of different data sets. Two steps were conducted in the inversion. First, surface wave dispersion and ZH ratio data were jointly inverted to obtain smooth V_S variations based on an initial model. The weights of both data sets were set to be equal.

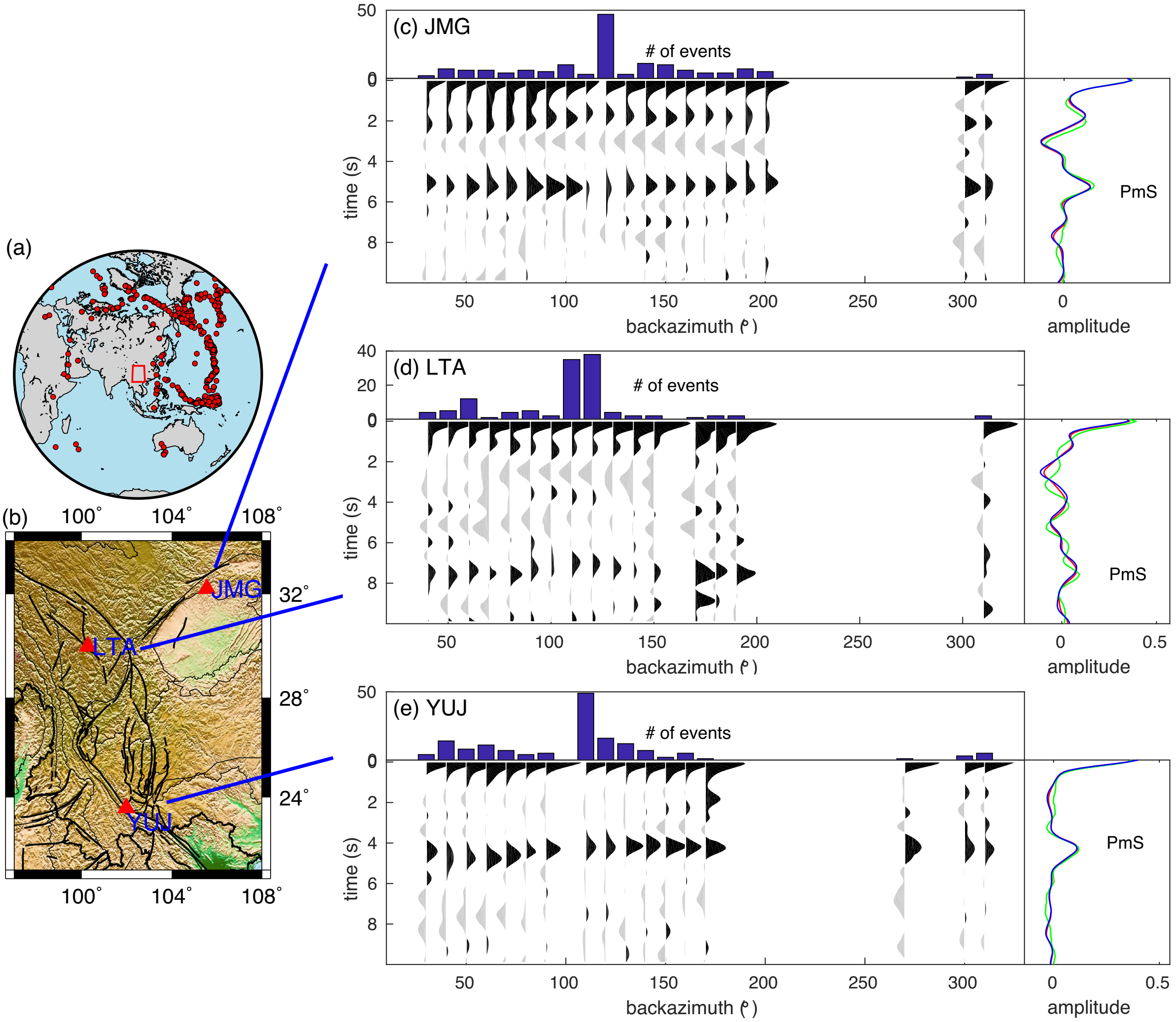

Figure 7. (a) Distribution of teleseismic events (red dots); the red rectangle denotes the study region. (b) Locations of the three example stations. (c)–(e) RF waveforms of the example stations, stacked in each 10° bin. The histograms on the top show the number of RFs for each stacked bin. The blue, green, red traces in the right-hand plot show the stacked RF over all traces, the azimuthally independent term $A(t)$ after harmonic decomposition, and the average of $H_i(\phi, t)$ between 30° and 150° azimuth range, respectively. The *P*-to-*S* conversions from the Moho (*Pms*) are marked.

Synthetic tests demonstrated that these values usually converged sufficiently after seven iterations. Secondly, RFs were incorporated with a larger weight in the joint inversion to obtain a finer V_S model based on the smooth value from the preceding step, in which better constraints on the interfaces were achieved. A total of 20 iterations were performed. The three data sets were primarily sensitive to V_S, so we only retrieved the V_S model with joint inversion. During this process, the V_P and density were computed from the V_S by the empirical relationships from Brocher (2005).

We interpolated the model from surface wave tomography (Shen *et al.* 2016) onto the location of each station to build a smooth initial reference model. The initial model was from the surface to the half space at the depth of 100 km. As stated in Section 2.4, the top 10 km of the Sichuan Basin initial velocity model was from Wang *et al.* (2016). For the model parametrization, we set a boundary 5-km deeper than the Moho in Shen *et al.* (2016). The thickness of the layers between the surface and this boundary was 2 km. The thickness of the layers between this boundary and the half space was 10 km. Such parametrization offers better vertical resolution in the crust than in the mantle. Meanwhile, variation in the Moho depth was also allowed at a fine scale in the joint inversion.

For the 114 stations with both RF and ZH ratio data available (Fig. 1a), we interpolated the phase velocity maps into dispersion curves at each station and then performed the stepwise joint inversion with three data for a 1-D V_S model beneath the station. We chose the smoothing parameter $\eta = 2$ for the first-order Tikhonov regularization. In the first step, we set the weighting coefficients of the dispersion and ZH ratio equal ($p = q = 0.5$). In the second step, we tested the weights for three data sets: $p = q = 0.2$ and $r = 0.6$ for the first and $p = q = 0.1$ and $r = 0.8$ for the second. For most stations, the two results showed little difference.

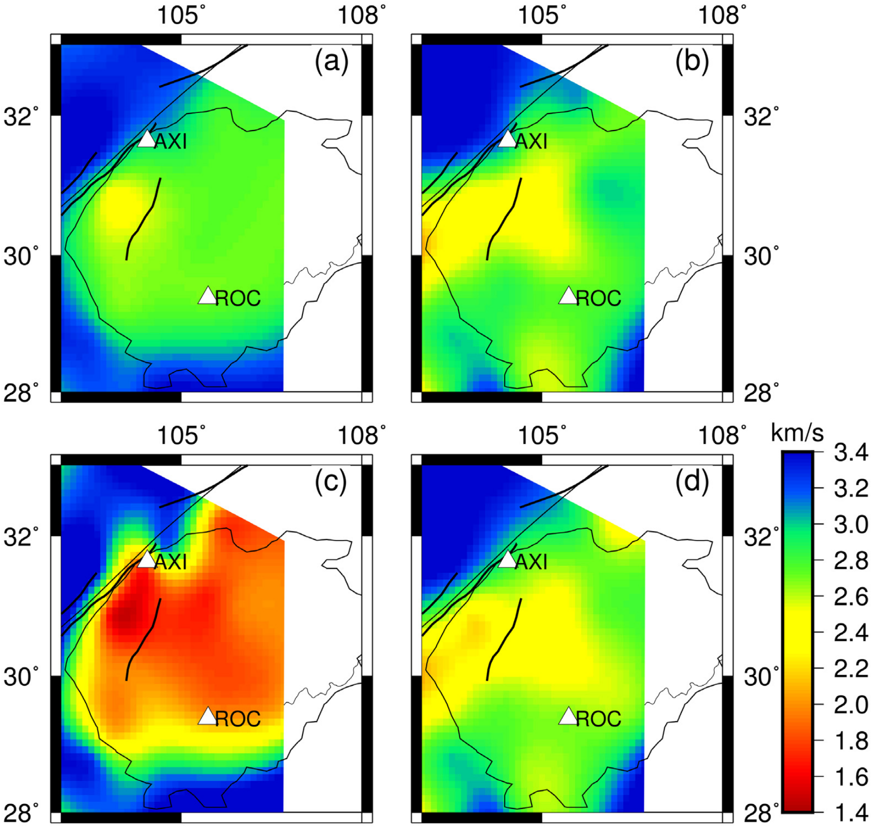

Figure 8. Absolute shear velocity at 1-km depth in the Sichuan Basin modified from Wang *et al.* (2016) (a) and Shen *et al.* (2016) (c). Panels (b) and (d) are the inversion results when using the initial model in (a) and (c), respectively. The white triangles show the locations of stations AXI and ROC, of which 1-D models are plotted in Fig. 9.

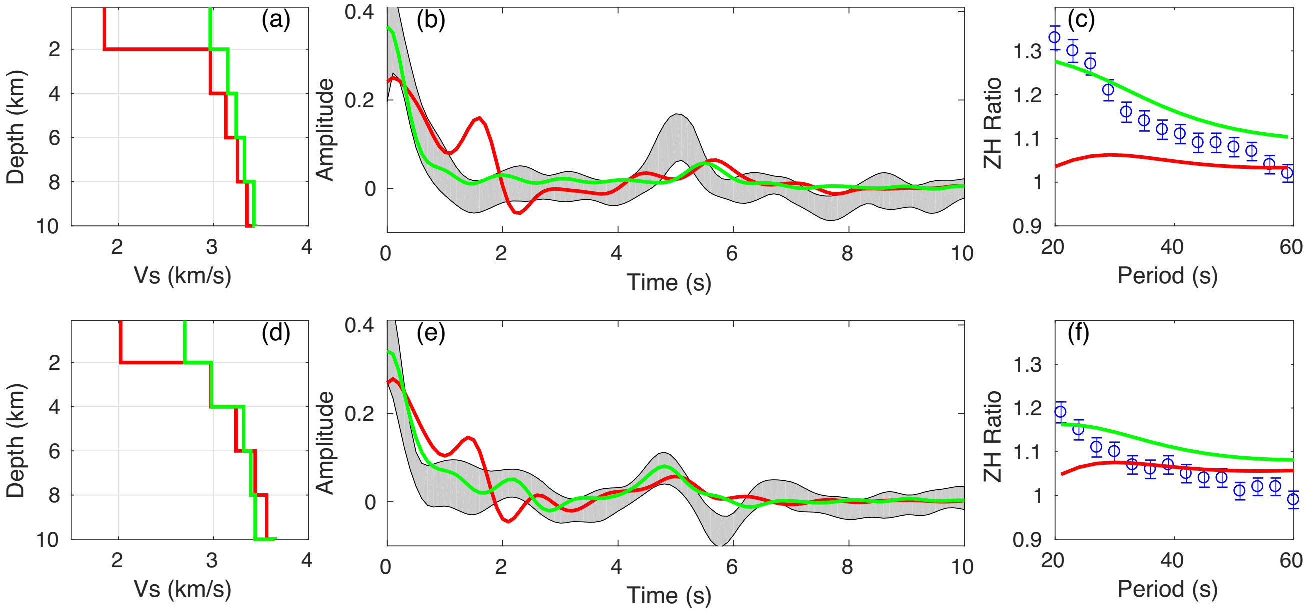

Figure 9. Comparison of the top 10-km V_S models and their data fitness based on surface waves (red lines, Shen *et al.* 2016) and sonic logging measurements (green lines, Wang *et al.* 2016) for stations AXI (a–c) and ROC (d–f). Panels (a) and (d) are the 1-D V_S model down to 10-km depth. Panels (b) and (e) are the observed RFs, with the uncertainties shown as grey shaded areas, and the predicted data with the two models. Panels (c) and (f) are the observed Rayleigh wave ZH ratios, with the uncertainties shown as blue bars, and the predicted data with the two models. The locations of stations AXI and ROC are shown in Fig. 8.

For some other stations, the RFs were overfitted with larger weight. Thus, we chose to use weights of $p = q = 0.2$ and $r = 0.6$. After the first step of the joint inversion, the Rayleigh wave dispersion and ZH ratio data of 11 stations were hard to adequately fit (blue-coded stations in Fig. 1a). Surface wave dispersion from ambient noise is more stable than ZH ratio measurements due to the amplitude response of the instruments. For the 11 stations, we replaced the raw measurements with the interpolated ZH ratios from surrounding stations. After the joint inversion with three data sets was performed for all 114 stations, we can roughly estimate the V_S errors in our model. We added random noise to the data according to the noise level of each data set and then performed the inversion for plenty of times, which we called the Monte Carlo error analysis (Zhang & Yao 2017). The inversion models from the 100 tests for station MGU, whose inversion result has the largest misfit, show consistent features (Fig. S2). The V_S errors of the layers range from 0.027 to 0.098 km s^{-1}. So we estimated that the V_S model error in our inversion result is less than 0.1 km s^{-1}. Finally, we interpolated the V_S models onto $0.5° \times 0.5°$ gridpoints at each 2-km depth to construct a 3-D V_S model.

4 RESULTS

Fig. 10 shows an example of the joint inversion with three data sets for station LTA (see Fig. 7b). Compared to the initial model, the final model displays a notably low V_S anomaly within a few kilometres in the uppermost crust (0–4 km) and low-velocity zones (LVZs) in the mid crust (∼20–30 km) (Fig. 10d). The synthetic data after joint inversion fit the observations much better than those from the initial model, especially for the Rayleigh wave ZH ratios and RF data (Figs 10b and c). More examples are shown in the supplementary material (Figs S3 and S4).

We only focus on the crustal and uppermost-mantle structures down to a depth of 70 km in the study region (Fig. 11), with relatively good constraints based on the sensitivities of the available data sets (e.g. Fig. 5). The upper-mantle structure (depth > 70 km) is poorly resolved and thus excluded in the interpretation, as the longest period for surface waves is 40 s for dispersion and 60 s for the ZH ratio. V_S maps at depths of 2, 10, 20, 30, 40 and 50 km in Fig. 11 show different patterns. At 2-km depth, the Sichuan and Chuxiong Basins are characterized by low V_S anomalies due to the presence of thick sediments. The low V_S anomaly of ∼2.5 km s^{-1} in the Sichuan Basin appears to be higher than that of the results from Shen *et al.* (2016). High V_S anomalies appear near the Xianshuihe fault and the Panzhihua area north of the Lüzhijiang fault. At 10-km depth, the northern portion of the Sichuan Basin remains the low V_S anomaly. The low V_S anomaly appears around the Xianshuihe fault and the Litang fault as well. The highest V_S anomaly correlates with the ELIP. At 20 km depth, the Longmenshan fault separates the high V_S anomaly in the Sichuan Basin from the low V_S anomaly in the Songpan-Ganzi fold belt. The ELIP maintains a higher V_S anomaly. Two prominent low-V_S anomalies are present at 30-km depth. One extends from the western side of the Xianshuihe and Lijiang-Xiaojinhe faults to the western side of the Red River fault, and the other appears around the Xiaojiang fault zone, which are observed as two low- V_S channels in (Bao *et al.* 2015). The large low-V_S anomaly from depths of 40 to 50 km is mainly related to variations in crustal thickness in this region (Wang *et al.* 2017). In the vertical cross sections, the mid-crustal LVZs approximately 20–30-km depth (contoured with 3.4 km s^{-1} in Fig. 12) are clearer.

5 DISCUSSION

5.1 Improvement of the shallow crustal structure by incorporating new data

Most recent crustal shear velocity models in SW China were proposed by traveltime tomography study (Xin *et al.* 2019), surface wave tomography study (Shen *et al.* 2016) and joint inversion of surface wave dispersion and RF (Liu *et al.* 2014; Bao *et al.* 2015). Xin *et al.* (2019) and Shen *et al.* (2016) presented the V_S model of the whole continental China, with fewer details due to the smooth parameters (see supplementary figures). Liu *et al.* (2014) and Bao *et al.* (2015) used very dense arrays to reveal finer structure, but their arrays did not cover the whole SW China region. Moreover, these studies had poor resolution for the structure near the surface because their data had weak sensitivity and sparse ray path coverage at shallow depths. Such weak constraints on the shallow crust might have caused bias when recovering the deep mid-lower crustal structure with a conventional inversion algorithm. Our results generally agree with the structure that was resolved by previous studies but exhibit improvement in terms of constraining the shallow crust by incorporating the ZH ratio and prior constraints in the Sichuan Basin from industrial data and sonic logs. Additionally, we provide a unified model that fits multiple data sets, whereas previous models displayed variable structural features and failed to recover three data sets simultaneously (e.g. Figs 9 and 10). Although our data originate from relatively sparse permanent stations (interstation spacing of ∼70 km), the depth and geometry of the LVZs appear to be well resolved with the joint inversion of three data sets compared to the results from the very dense array (interstation spacing of ∼35 km) by Bao *et al.* (2015, see supplementary material).

Fig. 8 displays the V_S models at 1-km depth in the Sichuan Basin from the initial models and their corresponding inversion results. The V_S of ∼2.5 km s^{-1} in the Sichuan Basin in our model is much higher than that of the model from Shen *et al.* (2016), which is lower than 2 km s^{-1} in most of the basin (Fig. 8c). The V_P model in the Sichuan Basin, which is derived from oil wells, industrial isopach maps, geological maps and a digital elevation model (Fig. 8a, Wang *et al.* 2016), reveals notably higher velocities than those in the regional tomography model when using local body-wave traveltime data (Lei & Zhao 2009). Because the Sichuan Basin generally lacks low-velocity Cenozoic sediments, the shallow portion of the basin is mainly covered by relatively old, more compacted Mesozoic sandstones and siltstones, thus exhibiting higher V_s than other typical sedimentary basins. Our inversion results with relatively high velocities in the sedimentary rocks (Fig. 8b) are comparable to other results (Fig. 8a), showing a good correlation with the geology. The inversion results with the two initial models show quite similar pattern of higher velocity material in the basin (Figs 8b and d). This result demonstrates that our inversion with three types of data has sufficient constraints on the shallow crustal structure and difference choices of initial models generally result in very similar inversion results, which has also been claimed in Zhang & Yao (2017).

5.2 Major velocity features in the new model

The widespread LVZs in the mid-lower crust in SW China, which are indicative of mechanically weak zones, have been demonstrated by geophysical evidences. However, studies using different data and methods revealed different depth and spatial-distribution patterns for these weak mid-lower crustal zones (e.g. Bai *et al.* 2010; Zhao *et al.* 2013; Huang *et al.* 2015; Qiao *et al.* 2018). Our inversion

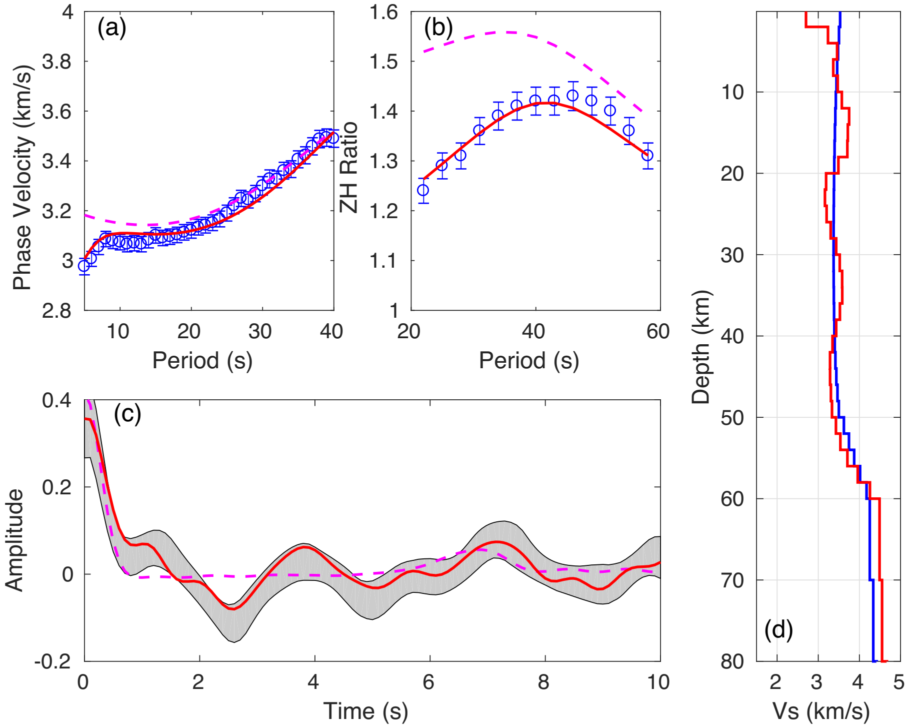

Figure 10. Example of the joint inversion at station LTA in the eastern Tibetan Plateau (see location in Fig. 7b). (a) Rayleigh wave phase velocities, with the uncertainties presented as blue error bars. (b) Rayleigh wave ZH ratio, with the uncertainties presented as blue error bars. (c) RFs, with the uncertainties shown as grey shaded areas. The red solid lines and magenta dashed lines in (a)–(c) correspond to the predicted data sets of the final model and initial model, respectively. (d) Initial model (blue) from W Shen et al. (2016) and final model (red) after the joint inversion.

results, which are constrained by more data sets, reveal mid-crustal LVZs with shallower depth and more complex spatial patterns. In the vertical cross sections (Fig. 12), we contour the LVZs with V_S values of 3.4 km s^{-1}, below which the existence of partial melting at 30-km depth is plausible (Yang *et al.* 2012). The most prominent low-velocity anomalies (inside the regions contoured with 3.4 km s^{-1}) are at a depth of 10–30 km (Fig. 12), shallower than previously suggested. The existence of partial melting is also likely at depths below 30 km in the lower crust, where the V_S values are significantly lower than the global average (e.g. approximately 3.8–3.9 km s $^{-1}$). The V_S map at 30-km depth (Fig. 11d) reveals two prominent low-velocity channels. The channel to the west extends southwestward from the northern Chuandian block to the west of the Lijiang-Xiaojinhe fault and Red River fault. The channel to the east is similar to that in most previous studies, beneath the Xiaojiangfault zone. The boundaries of the two channels correlate well with the major faults in this region, which emphasizes the importance of this major deep-penetrating faults in the tectonic evolution of SE Tibet (Yao *et al*. 2008, 2010; Liu *et al.* 2014).

The spatial variations in scale, strength and lateral continuity of these LVZs remain complicated. The western portions of the cross sections AA′ and BB′ and the northern portion of EE′, which corresponds to the northern Chuandian block, display large-scale, pronounced and continuous mid-crustal LVZs (Figs 12b, c and f). These LVZs become less clear towards the Songpan-Ganzi fold belt to the east and finally disappear around the Longmenshan fault and Anninghe fault (Figs 12b and c). Diffuse LVZs of comparatively small scale can be found in the cross sections to the south, corresponding to the southern Chuandian block (Figs 12d and e). Previous studies attributed the mechanically weak zone to partial melting from elevated temperatures in the thickened crust, shear heating, and asthenosphere upwelling (Hu *et al.* 2000; Bai *et al.* 2010; Yang *et al.* 2012). Therefore, these spatial variations in the scale and strength of the mid-crustal LVZs result from differences in crustal rheology, which implies that the crust deforms with significant lateral differences in this region. The more continuous and pronounced LVZ beneath the northern Chuandian block suggests that the middle crust is comparatively weak, which may have been related to magmatism in and flow from central Tibet (Liu *et al.* 2014).

Our model also reveals a prominent high-V_S anomaly roughly in the inner zone of the ELIP (Bao *et al.* 2015, Qiao *et al.* 2018) and the region around the Anninghe-Zemuhe fault zone (Fig. 1b). This high-V_S anomaly in the upper to middle crust extends down to 30 km and is surrounded by earthquakes (Figs 11b–d). In the vertical cross sections BB′, CC′ and FF′, this high-V_S anomaly that is bounded by earthquakes could also be seen clearly (Figs 12c, d and g). This observation confirms the existence of a mechanically strong crust and vertically coherent deformation in the inner zone of the ELIP. The more rigid crust from the inner zone of the ELIP to the region around the Anninghe-Zemuhe fault zone likely obstructs the southward expansion of crustal material to the region around the Lijiang-Xiaojinhe fault (Qiao *et al.* 2018). The transport of crustal material along the more rigid Anninghe-Zemuhe fault zones is likely accommodated by strike-slip faulting.

The major velocity features in our model confirm that crustal channel flow in the unevenly distributed mid-crustal weak zones and more rigid block extrusion via strike-slip faults both play important roles in the regional dynamics of the southeastern margin of the Tibetan Plateau from the late Miocene to the present (Liu *et al.* 2014; Qiao *et al.* 2018).

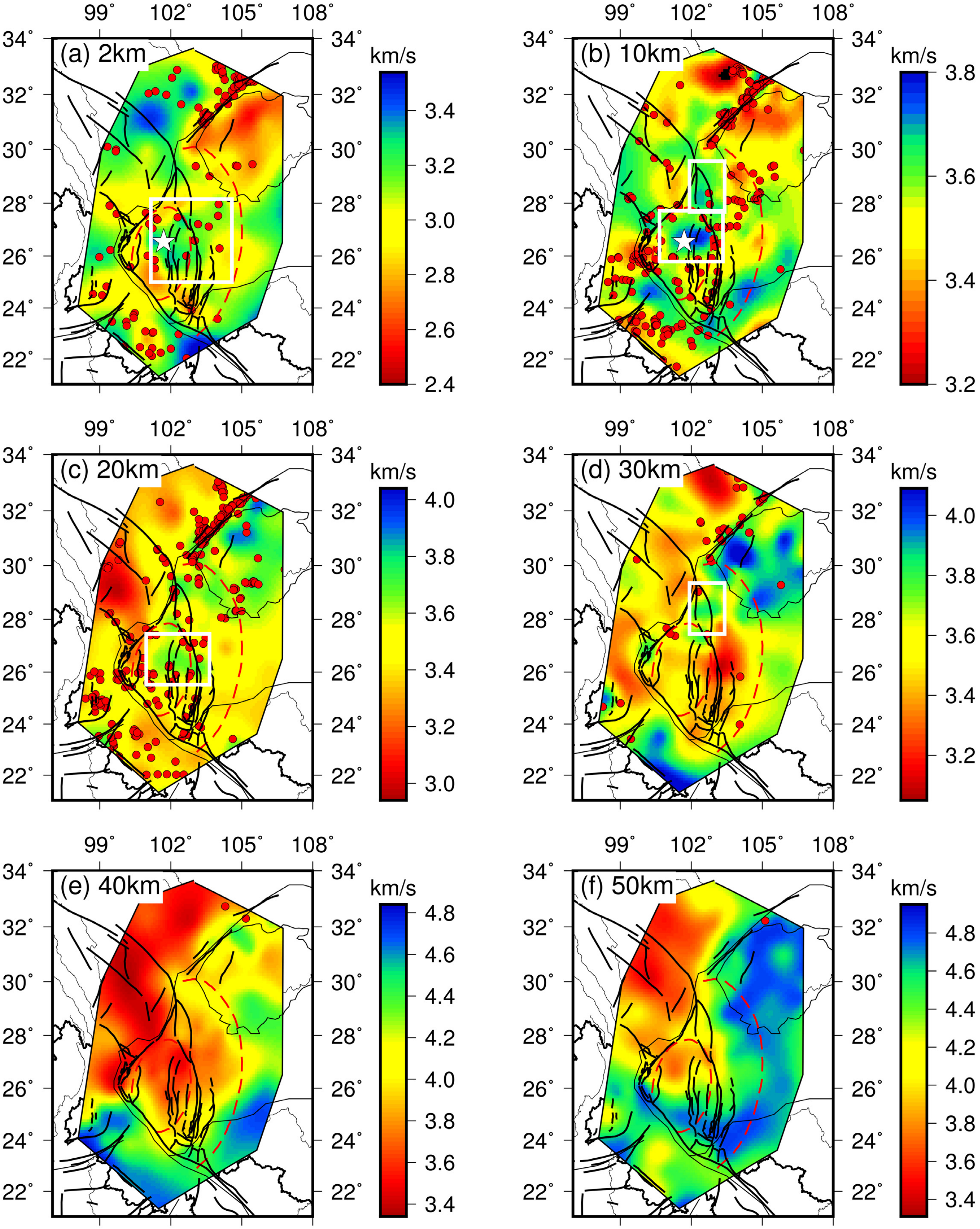

Figure 11. Variation in the absolute shear velocity at different depths. The thin black lines outline the block boundaries. The thick black lines represent major faults. The red dashed lines outline the boundary between the inner, intermediate and outer zones of the ELIP. The red dots show the epicentres of earthquakes ($M_w > 4$) at different depths. The white stars in (a) and (b) denote the location of the Panzhihua area. The white rectangles in (a–d) outline the high-velocity anomalies.

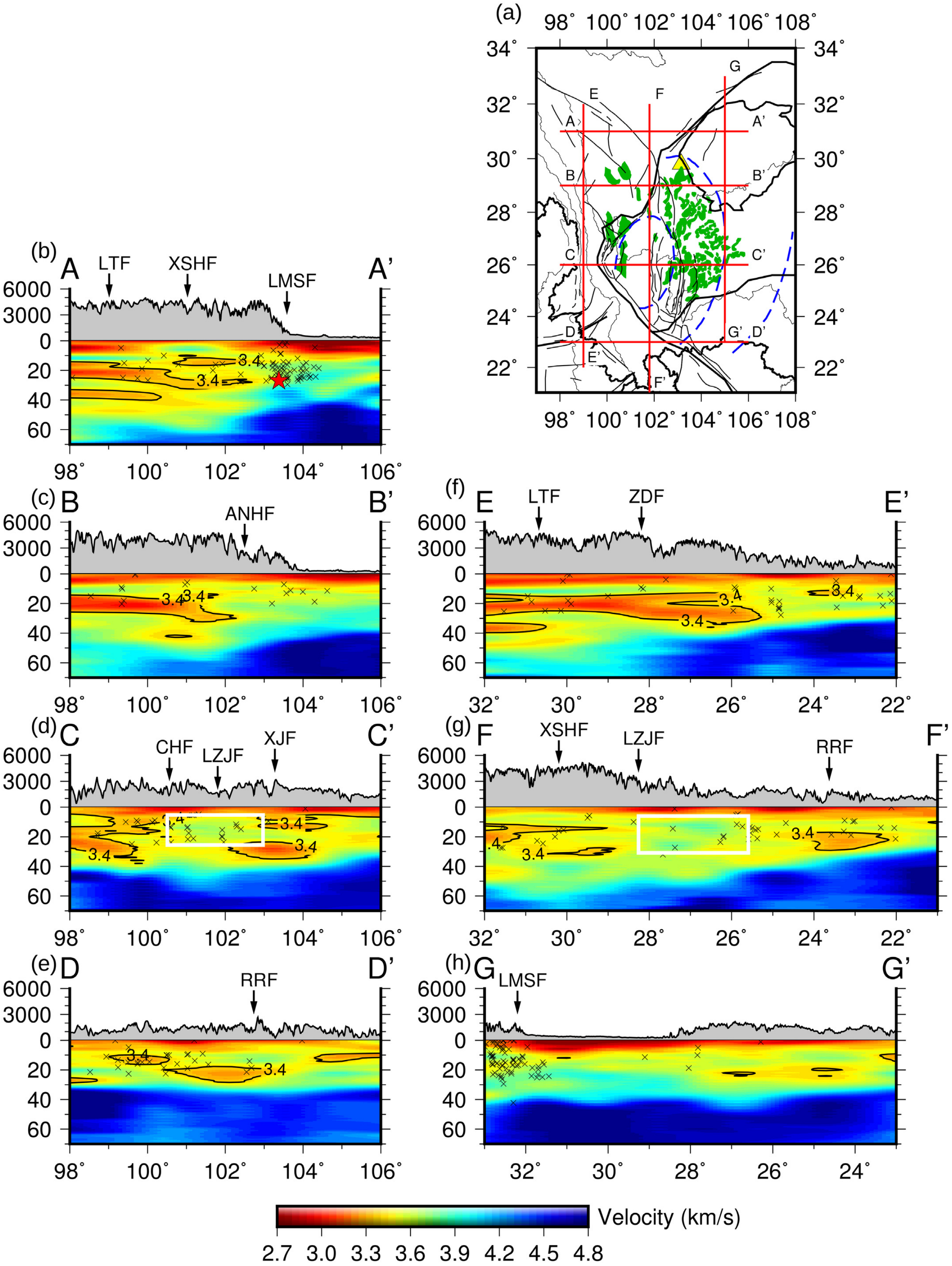

Figure 12. Seven vertical cross sections, which are represented by the red lines in (a). The green shaded area shows the distribution of the ELIP basalts (Y-G, Xu *et al*. 2004). The blue dashed lines outline the boundary between the inner, intermediate and outer zones of the ELIP. The shear wave velocity structures across the seven vertical cross sections in (a) are shown in (b)–(h), with the grey shaded areas above showing the topography along the cross sections. The black crosses denote the epicentres of earthquakes ($M_w > 5$) that occurred in 1980–2016. The red star represents the epicentre of the 2008 M_w 7.9 Wenchuan earthquake. The arrows above the topography plots denote the locations of major faults; the associated abbreviations are the same as those in Fig. 1. The white rectangles in (d) and (g) outline the high-velocity anomalies.

5.3 Lateral variations in crust–mantle transition zones

P-wave RFs can measure the 'sharpness' of crust–mantle transition zones (Owens & Zandt 1985; Julià 2007). Thick crust–mantle transition zones can be detected from Moho-converted Ps waves with small amplitude and long signal duration. With RF data incorporated into our joint inversion, our model could resolve lateral variations in crust–mantle transition zones. The western portions of the cross sections AA′ and BB′ and the northern portions of the cross sections EE′ and FF′ beneath the eastern Tibetan Plateau display relatively thick crust–mantle transition zones (Figs 12b, c, f and g). In contrast, the stable Sichuan Basin and southern Yunnan have a sharp crust–mantle boundary (Fig. 12). Previous studies revealed similar features (Liu *et al.* 2014). Thick crust–mantle transition zones could also be clearly seen between 101°E and 102°E in the cross section CC′ (Fig. 12d), which correspond to the inner zone of the ELIP.

Previous studies that were based on RF data also detected thick crust–mantle transition zones in some regions. Youssof *et al.* (2013) found good correspondence between the thicker crust–mantle transition zones and the thicker crust in high-topography areas in southern Africa. Levin *et al.* (2016) revealed a relatively unclear Moho beneath stations in Superior Province in North America, which underwent crustal reworking and extensive faulting in relation to continent–continent collision. Zheng *et al.* (2008) showed a gradual crust–mantle transition zone beneath the Taihangshan region in the central North China Craton, where significant lithospheric removal occurred. Therefore, thick crust–mantle transition zones are commonly related to active tectonics. Two possible causes could explain the thickening of these crust–mantle transition zones or the unclear Moho: (1) a 'top-down' mechanism, where the inflation and depression of weak material with partial melting in the mid-lower crust could lead to mixing and metasomatism in the crust–mantle transition zone, leading to a more unclear crust–mantle transition zone and (2) a 'bottom-up' mechanism, where mafic melt and heat from ascending upper-mantle material could result in the thermal/chemical erosion and thickening of these crust–mantle transition zones. To the north of our study region, the thick crust–mantle transition zones beneath the northern Chuandian block and the Songpan-Ganzi fold belt correlate well with the pronounced and continuous LVZs in the middle crust. The existence of significant mid-crustal partial melting seems to have a preference for the 'top-down' mechanism. In the inner zone of the ELIP, where our model reveals thick crust–mantle transition zone, *P*- and *S*-wave RF migration studies show deeper Moho but thinned lithosphere beneath the inner zone, alongside an additional interface in the lower crust and the absence of the Conrad discontinuity (Chen *et al.* 2015). Unlike southern Tibet, where crustal thickening can be explained by north–south crustal shortening (Yin & Harrison 2000), no evidence exists of significant crustal shortening around the ELIP. In contrast, most regions around the ELIP are currently undergoing east–west extension (He *et al.* 2003). If the crust is not thickened through crustal shortening, crustal thickening may have occurred at greater depths, which can be better explained by underplating from a mantle-plume-head melting model in the ELIP (Xu *et al.* 2004; Chen *et al.* 2015; Deng *et al.* 2016). The upwelling and underplating of intrusive mafic material from the plume head, matches the 'bottom-up' mechanism.

6 CONCLUSIONS

We used the joint inversion of Rayleigh wave dispersion from ambient noise, ZH ratios from earthquake surface waves, and *P*-wave RF data for 114 permanent stations and incorporated sonic logging measurements and velocity-analysis results in petroleum exploration in the initial model to present a new 3-D crustal shear velocity model beneath SW China. With complementary information from multiple data sets, this new model can better constrain the crustal structure in this region. Our new model can serve as a reference crustal model for construction of more high-resolution tomographic models or earthquake source studies in SW China. We also draw the following conclusions:

(1) Compared to previous tomography results, higher V_S in the sedimentary basins is observed beneath the Sichuan Basin, corresponding to direct velocity measurements by industrial data and sonic logs of old and compacted Mesozoic sedimentary rocks in the shallow Sichuan Basin.

(2) Our model reveals two mid-crustal low-velocity channels, the boundaries of which correlate well with the major fault system. Prominent high-velocity anomalies in the inner zone of the ELIP (which is surrounded by earthquakes) and the region around the Anninghe-Zemuhe fault zone indicate that the local, mechanically strong crust has obstructed southward crustal ductile flow.

(3) In contrast to the sharp Moho beneath the Yangtze craton, the northern Chuandian block and the inner zone of the ELIP have thick crustal–mantle transition zones, which result from 'top-down' inflation of partial melting material from the mid-lower crust and 'bottom-up' underplating from the mantle plume, respectively.

ACKNOWLEDGEMENTS

We appreciate the constructive comments from the two anonymous reviewers, which have helped us improve the quality and clarity of the original manuscript. We thank the Data Management Centre of China National Seismic Network at Institute of Geophysics, China Earthquake Administration for providing waveform data in SW China (doi:10.11998/SeisDmc/SN, http://www.seisdmc.ac.cn). All the Rayleigh wave dispersion, ZH ratio and receiver function data used in this paper are available by contacting H. Yao (hjyao@ustc.edu.cn) or Y. Yang (yangyan1995@hotmail.com). The crustal model for each station can be found on https://github.com/yanyangg/SW_China_Vs_model. This study is supported by China Earthquake Science Experiment Project, China Earthquake Administration (Project Codes: 2017CESE0101, 2018CSES0101), National Nature Science Foundation of China (grant number: 41790464, 41702202) and Nature Science Foundation of Jiangsu Province (BK20170868).

REFERENCES

Ali, J.R., Fitton, J.G. & Herzberg, C., 2010. Emeishan large igneous province (SW China) and the mantle-plume up-doming hypothesis, *J. Geol. Soc. Lond.,* **167,** 953–959.

Ammon, C.J., 1991. The isolation of receiver effects from teleseismic P waveforms, *Bull. seism. Soc. Am.,* **81,** 2504–2510.

Aster, R.C., Borchers, B. & Thurber, C.H., 2013. *Parameter Estimation and Inverse Problems,* 3rd edn, Elsevier, doi:10.1016/C2009-0-61134-X.

Bai, D. *et al.*, 2010. Crustal deformation of the eastern Tibetan plateau revealed by magnetotelluric imaging, *Nat. Geosci.,* **3,** 358, doi:10.1038/Ngeo830.

Bao, X., Sandvol, E., Ni, J., Hearn, T., Chen, Y.J. & Shen, Y., 2011. High resolution regional seismic attenuation tomography in eastern Tibetan Plateau and adjacent regions, *Geophys. Res. Lett.,* **38,** 129–135.

Bao, X. *et al.*, 2015. Two crustal low-velocity channels beneath SE Tibet revealed by joint inversion of Rayleigh wave dispersion and receiver functions, *Earth planet. Sci. Lett.,* **415,** 16–24.

Bensen, G.D., Ritzwoller, M.H., Barmin, M.P., Levshin, A.L., Lin, F., Moschetti, M.P., Shapiro, N.M. & Yang, Y., 2007. Processing seismic ambient noise data to obtain reliable broad-band surface wave dispersion measurements, *Geophys. J. Int.,* **169,** 1239–1260.

Brocher, T.M., 2005. Empirical relations between elastic wavespeeds and density in the Earth's crust, *Bull. seism. Soc. Am.,* **95,** 2081–2092.

Chen, Y. *et al.*, 2015. Magmatic underplating and crustal growth in the Emeishan Large Igneous Province, SW China, revealed by a passive seismic experiment, *Earth planet. Sci. Lett.,* **432,** 103–114.

Chong, J., Ni, S., Chu, R. & Somerville, P., 2016. Joint inversion of body-wave receiver function and rayleigh-wave ellipticity, *Bull. seism. Soc. Am.,* **106,** 537–551.

Clark, M.K. & Royden, L.H., 2000. Topographic ooze: building the eastern margin of Tibet by lower crustal flow, *Geology,* **28,** 703, doi:10.1130/0091-7613(2000)28.

Cook, K.L. & Royden, L.H., 2008. The role of crustal strength variations in shaping orogenic plateaus, with application to Tibet, *J. geophys. Res.,* **113,** doi:10.1029/2007JB005457.

Deng, Y., Chen, Y., Wang, P., Essa, K.S., Xu, T., Liang, X. & Badal, J., 2016. Magmatic underplating beneath the Emeishan large igneous province (South China) revealed by the COMGRA-ELIP experiment, *Tectonophysics,* **672,** 16–23.

Deng, Y., Zhang, Z., Mooney, W., Badal, J., Fan, W. & Zhong, Q., 2014. Mantle origin of the Emeishan large igneous province (South China) from the analysis of residual gravity anomalies, *Lithos,* **204,** 4–13.

Dziewonski, A.M. & Anderson, D.L., 1981. Preliminary reference Earth model, *Phys. Earth planet. Inter.,* **25,** 297–356.

Eagar, K.C. & Fouch, M.J., 2012. FuncLab: a MATLAB interactive toolbox for handling receiver function datasets, *Seismol. Res. Lett.,* **83,** 596–603.

Ferreira, A.M.G. & Woodhouse, J.H., 2007. Observations of long period Rayleigh wave ellipticity, *Geophys. J. Int.,* **169,** 161–169.

He, B., Xu, Y.-G., Chung, S.-L., Xiao, L. & Wang, Y., 2003. Sedimentary evidence for a rapid, kilometer-scale crustal doming prior to the eruption of the Emeishan flood basalts, *Earth planet. Sci. Lett.,* **213,** 391–405.

Huang, H., Yao, H. & van der Hilst, R.D., 2010. Radial anisotropy in the crust of SE Tibet and SW China from ambient noise interferometry, *Geophys. Res. Lett.,* **37,** 193–195.

Huang, J., Zhao, D. & Zheng, S., 2002. Lithospheric structure and its relationship to seismic and volcanic activity in southwest China, *J. geophys. Res.,* **107,** ESE 13–11-ESE 13-14.

Huang, Z. *et al.*, 2015. Mantle structure and dynamics beneath SE Tibet revealed by new seismic images, *Earth planet. Sci. Lett.,* **411,** 100–111.

Hu, J., Badal, J., Yang, H., Li, G. & Peng, H., 2018. Comprehensive crustal structure and seismological evidence for lower crustal flow in the southeastern margin of Tibet revealed by receiver functions, *Gondwana Res.,* **55,** 42–59.

Hu, S., He, L. & Wang, J., 2000. Heat flow in the continental area of China: a new data set, *Earth planet. Sci. Lett.,* **179,** 407–419.

Jiang, G., Hu, S., Shi, Y., Zhang, C., Wang, Z. & Hu, D., 2019. Terrestrial heat flow of continental China: Updated dataset and tectonic implications, *Tectonophysics,* **753,** 36–48.

Julià, J., 2007. Constraining velocity and density contrasts across the crust-mantle boundary with receiver function amplitudes, *Geophys. J. Int.,* **171,** 286–301.

Julià, J., Ammon, C.J., Herrmann, R.B. & Correig, A.M., 2000. Joint inversion of receiver function and surface wave dispersion observations, *Geophys. J. Int.,* **143,** 99–112.

Kang, D., Shen, W., Ning, J. & Ritzwoller, M.H., 2016. Seismic evidence for lithospheric modification associated with intracontinental volcanism in Northeastern China, *Geophys. J. Int.,* **204,** 215–235.

Kennett, B.L.N.N. & Engdahl, E.R., 1991. Traveltimes for global earthquake location and phase identification, *Geophys. J. Int.,* **105,** 429–465.

Lei, J. & Zhao, D., 2009. Structural heterogeneity of the Longmenshan fault zone and the mechanism of the 2008 Wenchuan earthquake (Ms 8.0), *Geochem., Geophys. Geosyst.,* **10,** doi:10.1029/2009gc002590.

Levin, V., VanTongeren, J.A. & Servali, A., 2016. How sharp is the sharp Archean Moho? Example from eastern Superior Province, *Geophys. Res. Lett.,* **43,** 1928–1933.

Li, H., Su, W., Wang, C.Y. & Huang, Z., 2009. Ambient noise Rayleigh wave tomography in western Sichuan and eastern Tibet, *Earth planet. Sci. Lett.,* **282**(1−4), 201–211.

Lin, F.C., Schmandt, B. & Tsai, V.C., 2012. Joint inversion of Rayleigh wave phase velocity and ellipticity using USArray: constraining velocity and density structure in the upper crust, *Geophys. Res. Lett.,* **39**(12), doi:10.1029/2012GL052196.

Liu, C. & Yao, H., 2017. Surface wave tomography with spatially varying smoothing based on continuous model regionalization, *Pure appl. Geophys.,* **174,** 937–953.

Liu, Q.Y. *et al.*, 2014. Eastward expansion of the Tibetan Plateau by crustal flow and strain partitioning across faults, *Nat. Geosci.,* **7,** 361–365.

Liu, Z., Park, J. & Rye, D.M., 2015. Crustal anisotropy in northeastern Tibetan Plateau inferred from receiver functions: rock textures caused by metamorphic fluids and lower crust flow? *Tectonophysics,* **661,** 66–80.

Molnar, P. & Tapponnier, P., 1975. Cenozoic tectonics of Asia: effects of a continental collision: features of recent continental tectonics in Asia can be interpreted as results of the India-Eurasia collision, *Science,* **189,** 419–426.

Nguyen, V.-D., Huang, B.-S., Le, T.-S., Dinh, V.-T., Zhu, L. & Wen, K.-L., 2013. Constraints on the crustal structure of northern Vietnam based on analysis of teleseismic converted waves, *Tectonophysics,* **601,** 87–97.

Owens, T.J. & Zandt, G., 1985. The response of the continental crust-mantle boundary observed on broadband teleseismic receiver functions, *Geophys. Res. Lett.,* **12,** 705–708.

Qiao, L., Yao, H., Lai, Y., Huang, B. & Zhang, P., 2018. Crustal structure of southwest china and northern vietnam from ambient noise tomography: implication for the large-scale material transport model in SE Tibet, *Tectonics,* **37,** 1492–1506.

Rippe, D. & Unsworth, M., 2010. Quantifying crustal flow in Tibet with magnetotelluric data, *Phys. Earth planet. Inter.,* **179,** 107–121.

Royden, L.H., 1997. Surface deformation and lower crustal flow in Eastern Tibet, *Science,* **276,** 788–790.

Royden, L.H., Burchfiel, B.C. & van der Hilst, R.D., 2008. The geological evolution of the Tibetan Plateau, *Science,* **321,** 1054–1058.

Shen, F., Royden, L.H. & Burchfiel, B.C., 2001. Large-scale crustal deformation of the Tibetan Plateau, *J. geophys. Res.,* **106,** 6793–6816.

Shen, W., Ritzwoller, M.H., Schulte-Pelkum, V. & Lin, F.-C., 2013. Joint inversion of surface wave dispersion and receiver functions: a Bayesian Monte-Carlo approach, *Geophys. J. Int.,* **192,** 807–836.

Shen, W. *et al.*, 2016. A seismic reference model for the crust and uppermost mantle beneath China from surface wave dispersion, *Geophys. J. Int.,* **206,** 954–979.

Snieder, R., 2004. Extracting the Green's function from the correlation of coda waves: a derivation based on stationary phase, *Phys. Rev. E,* **69,** doi:10.1103/PhysRevE.69.046610.

Tanimoto, T. & Rivera, L., 2008. The ZH ratio method for long-period seismic data: sensitivity kernels and observational techniques, *Geophys. J. Int.,* **172,** 187–198.

Tapponnier, P., Peltzer, G., Dain, A.Y.Le, Armijo, R. & Cobbold, P., 1982. Propagating extrusion tectonics in Asia: new insights from simple experiments with plasticine, *Geology,* **10,** 611–616.

Tapponnier, P., Zhiqin, X., Roger, F., Meyer, B., Arnaud, N., Wittlinger, G. & Jingsui, Y., 2001. Oblique stepwise rise and growth of the Tibet Plateau, *Science,* **294,** 1671–1677.

Tarantola, A. & Valette, B., 1982. Generalized nonlinear inverse problems solved using the least squares criterion, *Rev. Geophys.,* **20,** 219, doi:10.1029/RG020i002p00219.

Wang, C., Chan, W.W. & Mooney, W.D., 2003. Three-dimensional velocity structure of crust and upper mantle in southwestern China and its tectonic implications, *J. geophys. Res.,* **108,** doi:10.1029/2002JB001973.

Wang, C., Han, W., Wu, J., Lou, H. & Chan, W.W., 2007. Crustal structure beneath the eastern margin of the Tibetan Plateau and its tectonic implications, *J. geophys. Res.,* **112,** B07307, doi:10.1029/2005JB003873.

Wang, E., 1998. *Late Cenozoic Xianshuihe-Xiaojiang, Red River, and Dali fault systems of southwestern Sichuan and central Yunnan, China,* Geological Society of America.

Wang, E. & Burchfiel, B.C., 2000. Late Cenozoic to Holocene deformation in southwestern Sichuan and adjacent Yunnan, China, and its role in formation of the southeastern part of the Tibetan Plateau, *Bull. geol. Soc. Am.,* **112,** 413–423.

Wang, M., Hubbard, J., Plesch, A., Shaw, J.H. & Wang, L., 2016. Three-dimensional seismic velocity structure in the Sichuan basin, China, *J. geophys. Res.,* **121,** 1007–1022.

Wang, W., Wu, J., Fang, L., Lai, G. & Cai, Y., 2017. Crustal thickness and Poisson's ratio in southwest China based on data from dense seismic arrays, *J. geophys. Res.,* **122,** 7219–7235.

Xin, H., Zhang, H., Kang, M., He, R., Gao, L. & Gao, J., 2019. High-resolution lithospheric velocity structure of continental china by double-difference seismic travel-time tomography, *Seismol. Res. Lett.,* **90,** 229–241.

Xu, T., Zhang, Z., Liu, B., Chen, Y., Zhang, M., Tian, X., Xu, Y. & Teng, J., 2015. Crustal velocity structure in the Emeishan large igneous province and evidence of the Permian mantle plume activity, *Sci. China Earth Sci.,* **58,** 1133–1147.

Xu, Y.-G. & Chung, S.-L., 2001. The Emeishan large igneous province: evidence for mantle plume activity and melting conditions, *Geochimica,* **30,** 1–9.

Xu, Y.-G., He, B., Chung, S.-L., Menzies, M.A. & Frey, F.A., 2004. Geologic, geochemical, and geophysical consequences of plume involvement in the Emeishan flood-basalt province, *Geology,* **32,** 917, doi:10.1130/G20602.1.

Yang, Y., Ritzwoller, M.H., Zheng, Y., Shen, W., Levshin, A.L. & Xie, Z., 2012. A synoptic view of the distribution and connectivity of the mid-crustal low velocity zone beneath Tibet, *J. geophys. Res.,* **117,** doi:10.1029/2011JB008810.

Yano, T., Tanimoto, T. & Rivera, L., 2009. The ZH ratio method for long-period seismic data: inversion for S-wave velocity structure, *Geophys. J. Int.,* **179,** 413–424.

Yao, H., Beghein, C. & Van Der Hilst, R.D., 2008. Surface wave array tomography in SE Tibet from ambient seismic noise and two-station analysis-II. Crustal and upper-mantle structure, *Geophys. J. Int.,* **173,** 205–219.

Yao, H., Gouedard, P., Collins, J.A., McGuire, J.J. & van der Hilst, R.D., 2011. Structure of young East Pacific Rise lithosphere from ambient noise correlation analysis of fundamental-and higher-mode Scholte-Rayleigh waves, *Comptes Rendus Geosci.,* **343,** 571–583.

Yao, H., van der Hilst, R.D. & de Hoop, M.V., 2006. Surface-wave array tomography in SE Tibet from ambient seismic noise and two-station analysis - I. Phase velocity maps, *Geophys. J. Int.,* **166,** 732–744.

Yao, H., van der Hilst, R.D. & Montagner, J.-P., 2010. Heterogeneity and anisotropy of the lithosphere of SE Tibet from surface wave array tomography, *J. geophys. Res.,* **115,** B12307, doi:10.1029/2009JB007142.

Yin, A. & Harrison, T.M., 2000. Geologic evolution of the Himalayan-Tibetan Orogen, *Annu. Rev. Earth planet. Sci.,* **28,** 211–280.

Youssof, M., Thybo, H., Artemieva, I.M. & Levander, A., 2013. Moho depth and crustal composition in Southern Africa, *Tectonophysics,* **609,** 267–287.

Yuan, Y., Yao, H. & Qin, Y., 2016. Joint inversion of rayleigh wave vertical-horizontal amplitude ratios and dispersion based on the neighborhood algorithm and its application, *Chinese J. Geophys.,* **59,** 139–152.

Zhang, P., 2013. A review on active tectonics and deep crustal processes of the Western Sichuan region, eastern margin of the Tibetan Plateau, *Tectonophysics,* **584,** 7–22.

Zhang, P., Deng, Q., Zhang, G., Ma, J., Gan, W., Min, W., Mao, F. & Wang, Q., 2003. Active tectonic blocks and strong earthquakes in the continent of China, *Sci. China Ser. D Earth Sci.,* **46,** 13–24.

Zhang, P. & Yao, H., 2017. Stepwise joint inversion of surface wave dispersion, Rayleigh wave ZH ratio, and receiver function data for 1D crustal shear wave velocity structure, *Earthq. Sci.,* **30,** 229–238.

Zhang, P. *et al.*, 2004. Continuous deformation of the Tibetan Plateau from global positioning system data, *Geology,* **32,** 809–812.

Zhang, X. & Wang, Y., 2009. Crustal and upper mantle velocity structure in Yunnan, Southwest China, *Tectonophysics,* **471,** 171–185.

Zhang, Y. *et al.*, 2018. 3-D crustal shear-wave velocity structure of the Taiwan Strait and Fujian, SE China, revealed by ambient noise tomography, *J. geophys. Res.,* **123,** 8016–8031.

Zhang, Z., Deng, Y., Teng, J., Wang, C., Gao, R., Chen, Y. & Fan, W., 2011. An overview of the crustal structure of the Tibetan plateau after 35 years of deep seismic soundings, *J. Asian Earth Sci.,* **40,** 977–989.

Zhang, Z., Yuan, X., Chen, Y., Tian, X., Kind, R., Li, X. & Teng, J., 2010. Seismic signature of the collision between the east Tibetan escape flow and the Sichuan Basin, *Earth planet. Sci. Lett.,* **292,** 254–264.

Zhao, L.-F., Xie, X.-B., He, J.-K., Tian, X. & Yao, Z.-X., 2013. Crustal flow pattern beneath the Tibetan Plateau constrained by regional Lg-wave Q tomography, *Earth planet. Sci. Lett.,* **383,** 113–122.

Zheng, T.Y., Zhao, L. & Zhu, R.X., 2008. Insight into the geodynamics of cratonic reactivation from seismic analysis of the crust-mantle boundary, *Geophys. Res. Lett.,* **35,** L08303, doi:10.1029/2008GL033439.

Zheng, X.-F., Yao, Z.-X., Liang, J.-H. & Zheng, J., 2010. The role played and opportunities provided by IGP DMC of China National Seismic Network in Wenchuan earthquake disaster relief and researches, *Bull. seism. Soc. Am.,* **100,** 2866–2872.

SUPPORTING INFORMATION

Supplementary data are available at *GJI* online.

The supplementary material contains six figures to illustrate some information in the main text. Fig. S1 is the phase velocity map at 5–40 s periods. Fig. S2 shows the Monte Carlo error analysis (Zhang & Yao 2017) for station MGU. Figs. S3 and S4 are the joint inversion results of the two stations that were mentioned in the main text. Fig. S5 and Fig. S6 shows shear-wave velocity cross sections of traveltime tomography study (Xin *et al.* 2019) and surface wave tomography study (Shen *et al.* 2016), respectively. Figs. S7 and S8 show six shear-velocity cross sections for a comparison between our model and a recent model that used the joint inversion of surface wave dispersion and receiver function (Bao *et al.* 2015).